

OPEN ACCESS

Ambient Ammonia Electrosynthesis from Nitrogen and Water by Incorporating Palladium in Bimetallic Gold–Silver Nanocages

To cite this article: Mohammadreza Nazemi et al 2020 J. Electrochem. Soc. 167 054511

View the <u>article online</u> for updates and enhancements.





Ambient Ammonia Electrosynthesis from Nitrogen and Water by Incorporating Palladium in Bimetallic Gold-Silver Nanocages

Mohammadreza Nazemi, 1,2,*,z Luke Soule, 3,* Meilin Liu, 3,** and Mostafa A. El-Sayed 1,z

¹Laser Dynamics Laboratory, School of Chemistry and Biochemistry, Georgia Institute of Technology, Atlanta, Georgia 30332-0400, United States of America

²George W. Woodruff School of Mechanical Engineering, Georgia Institute of Technology, Atlanta, Georgia 30332-0405, United States of America

³School of Materials Science and Engineering, Georgia Institute of Technology, Atlanta, Georgia 30332-0405, United States of America

Electrosynthesis of ammonia using nitrogen and water provides a potential alternative to the thermochemical process (Haber-Bosch) in a clean, sustainable, and decentralized way when electricity is generated from renewable sources. To enable the widespread commercialization of this technology, an electrocatalyst to convert nitrogen (N_2) to ammonia (N_3) with high selectivity and activity must be developed. Here, we report our findings in the investigation into the role of incorporating palladium (P_3 d) in bimetallic Au-Ag nanocages on the electrocatalytic activity of the nitrogen reduction reaction (N_3) under ambient conditions. The localized surface plasmon resonance (LSPR) peak position of the resulting trimetallic nanoparticles is tuned with N_3 0 using Au-Ag-Pd-850 nanoparticles at N_3 1 v vs RHE. This activity corresponds to the production energy efficiency of 28.9% with an electrical energy input of 19.1 MWh / ton N_3 1. The enhanced N_3 2 activity is attributed mainly to the formation of a highly porous N_3 3 is used to probe the mechanism of N_3 4 on the trimetallic nanostructures and to identify the intermediate species at the electrode-electrolyte interface.

© 2020 The Author(s). Published on behalf of The Electrochemical Society by IOP Publishing Limited. This is an open access article distributed under the terms of the Creative Commons Attribution 4.0 License (CC BY, http://creativecommons.org/licenses/by/4.0/), which permits unrestricted reuse of the work in any medium, provided the original work is properly cited. [DOI: 10.1149/1945-7111/ab6ee9]

Manuscript submitted October 24, 2019; revised manuscript received January 14, 2020. Published February 3, 2020. This was paper 2220 presented at the Atlanta, Georgia, Meeting of the Society, October 13–17, 2019. This paper is part of the JES Focus Issue on Heterogeneous Functional Materials for Energy Conversion and Storage.

Supplementary material for this article is available online

Ammonia is one of the most widely produced commodities in the world, with 146 million tons being produced globally in 2015 with an estimated increase in production of 3%–5% per year. Ammonia is used in numerous applications, most notably as a vital agrochemical and as a precursor for pharmaceutical products. ²⁻⁴ In addition to its widespread utility, ammonia also holds great promise as a carbonneutral liquid fuel for storing intermittent renewable energy sources when supply exceeds demand in the grid as well as for power generation due to the compound's high energy density (5.6 MWh ton⁻¹) and hydrogen content (17.6 wt%). ⁵ The conventional thermochemical process (i.e., Haber-Bosch process) for ammonia synthesis is capital- and energy-intensive, consuming 1%–2% of the global annual energy supply and 60% of the worldwide hydrogen production, and it emits 1%–2% of global CO₂ annually. ^{1,6} Renewably derived electrochemical synthesis of ammonia could provide a clean, sustainable, and decentralized route to the thermochemical process. ⁷

The lack of an active electrocatalyst to convert N_2 to NH_3 with high selectivity and activity is a bottleneck for the large scale electrosynthesis of ammonia under ambient conditions. Single-atom and hybrid Au electrocatalysts have shown relatively high activity due to the ability of Au to strongly adsorb and break $N\equiv N$ through the associative mechanism, with further sequential hydrogenation to form adsorbed N_2H_x species (1 < x < 4); the rate-determining step is N_2 dissociation (reduction of N_2^* to generate N_2H^*). Since N_2 It has been demonstrated that the rate-determining step kinetics is accelerated on transition metal hydrides, where H^* species on the catalyst surface directly react with the dissolved nitrogen in the electrolyte to form N_2H^* . Since N_2H^* is addition, a lithium mediated strategy (N_2H^*) in addition, a lithium mediated strategy (N_2H^*) in the transition metal catalyst could enhance the

electrochemical NRR activity at low temperatures due to lithium's unique ability to break the nitrogen triple bond, followed by hydrogenation to generate ammonia.^{18–20}

In our previous studies, we demonstrated the use of shape and pore-size controlled Au and bimetallic Au-Ag nanocages, with tunable localized surface plasmon resonance (LSPR) peak positions, as electrocatalysts for ammonia synthesis in an ionic aqueous solution with Faradaic efficiency >35%. The optimization of the structure, morphology, and composition is critical to enhancing the rate of electro-reduction of N_2 to NH_3 . We found that Au is catalytically more active than Ag in both photo- and electrochemical NRR. 22,24 Therefore, it is desired to replace Ag with another catalytic transition metal with higher NRR activity. This new metal must correctly modify the electronic structure of the nanoparticles by shifting the d-band center to ensure the optimum binding energy of an adsorbed species on the catalyst surface.²⁵ It was demonstrated that the electrochemical NRR takes place on the surface of Pd catalyst through the formation of Pd hydrides (PdH_x) at low overpotentials, followed by surface hydrogenation reactions. 17 The formation of PdH_x could weaken Pd –H bonding (proton adsorption strength on the Pd surface), leading to enhanced binding of Pd surface with N₂ and N-containing adsorbates. Here, we aim to investigate the role of incorporating palladium into bimetallic Au-Ag nanostructures on the electrocatalytic NRR activity in 0.5 M LiClO₄ (aq.) solution. Since the reduction potential of Pd (\sim 0.65 V vs RHE) is higher than that of Ag (\sim 0.5 V vs RHE) but lower than that of Au (∼1.2 V vs RHE), Ag can only be replaced with Pd in the galvanic replacement process after the addition of Pd salt (K₂PdCl₄ (aq.)) in the bimetallic Au-Ag nanostructures template. The red shifting of the LSPR peak position of the trimetallic nanostructures indicates either the replacement of Ag with Pd or the growth of Pd on Au. We also report energy input (MWh ton^{-1}_{NH3}) and production energy efficiency (%) of ammonia in the N_2 electrolysis system using our synthesized nanocatalysts, and we compare our results with the state-of-the-art Haber-Bosch system.

^{*}Electrochemical Society Student Member.

^{**}Electrochemical Society Fellow.

^zE-mail: mrnazemi@gatech.edu; melsayed@gatech.edu

In situ and operando surface-enhanced spectroscopy is a technique well suited to probe electrochemical reactions at the electrode/ electrolyte interface, and several studies have shown a great success for studying electrocatalytic water splitting and CO₂ reduction reactions. ^{26–28} Recently, surface-enhanced infrared absorption spectroscopy (SEIRAS) was used to determine electrocatalytic NRR mechanisms on Au and Pt surfaces. ²⁹ Operando surface enhanced Raman spectroscopy (SERS) allows for the detection of intermediate species even in low abundance and is used for the determination of NRR mechanisms using trimetallic Au-Ag-Pd nanostructures.

Results and Discussion

Bimetallic porous Au-Ag nanocages with an LSPR peak position at 650 nm are synthesized by the galvanic replacement method by adding HAuCl₄ (aq.) solution to a solution of solid silver nanocubes (AgNCs) (Figs. 1a and 1b). ^{21–24} Trimetallic Au-Ag-Pd nanostructures are synthesized by adding K₂PdCl₄ (aq.) solution to the porous bimetallic Au-Ag nanocages dispersed in DI water with the LSPR peak at 650 nm. The volume of the Pd²⁺ precursor added to the Au-Ag template, and subsequent reduction of Pd²⁺ to Pd⁰ (two Ag atoms are replaced with one palladium atom), is controlled by measuring the redshift in the LSPR peak positions of nanoparticles. As the amount of Pd salt solution increases, the amount of redshift and the LSPR bandwidth increases (Fig. 1a). Excessive addition of Pd salt results in aggregation and collapsing of the nanocages. The LSPR peak of the resulting trimetallic Au-Ag-Pd redshifts from

650 nm to 850 nm; indicating the replacement of the remaining Ag atoms in the Au-Ag nanocages with Pd atoms (galvanic replacement) or the growth of Pd on Au (Fig. 1). Due to the lattice mismatch between Pd (3.890 Å) and Au (4.079 Å), when Pd²⁺ precursor is added to the solution of Au-Ag nanocages, islands of palladium are formed on the Au surface. By further addition of the Pd salt solution, the islands are grown more, building a highly rough and porous surface (Figs. 1c and 1d).

Scanning transmission electron microscopy (STEM) and energy dispersive X-ray (EDX) spectroscopy are performed on a single trimetallic nanostructure to determine the structure, the elemental composition, and distribution of Au-Ag-Pd-750 and Au-Ag-Pd-850 nanoparticles (Fig. 2). For Au-Ag-Pd-750, Pd islands are distributed in the Au-Ag nanocages structure, indicating the successful incorporation of Pd into bimetallic Au-Ag nanocages, and the synthesis of trimetallic Au-Ag-Pd nanoparticles (Figs. 2a-2f). By increasing the amount of Pd salt solution and red shifting the LSPR peak from 750 nm to 850 nm, a continuous porous layer of Pd is formed at the exterior surface of the nanoparticles (Figs. 2g-2l). In addition, inductively coupled plasma emission spectroscopy (ICPES) measurements reveal that by adding the Pd salt solution into the Au-Ag nanocages, the Au content remains relatively unchanged while the Ag content decreases from 2.68 mg l^{-1} to 1.35 mg l^{-1} when the LSPR peak redshifts from 650 nm to 850 nm (Table I). This indicates that the galvanic replacement of Ag atoms with Pd ions is one of the mechanisms for the reduction of Pd^{2+} to Pd^0 in which the concentration of Pd increases to 1.23 mg l⁻¹ and 2.77 mg l⁻¹ as the

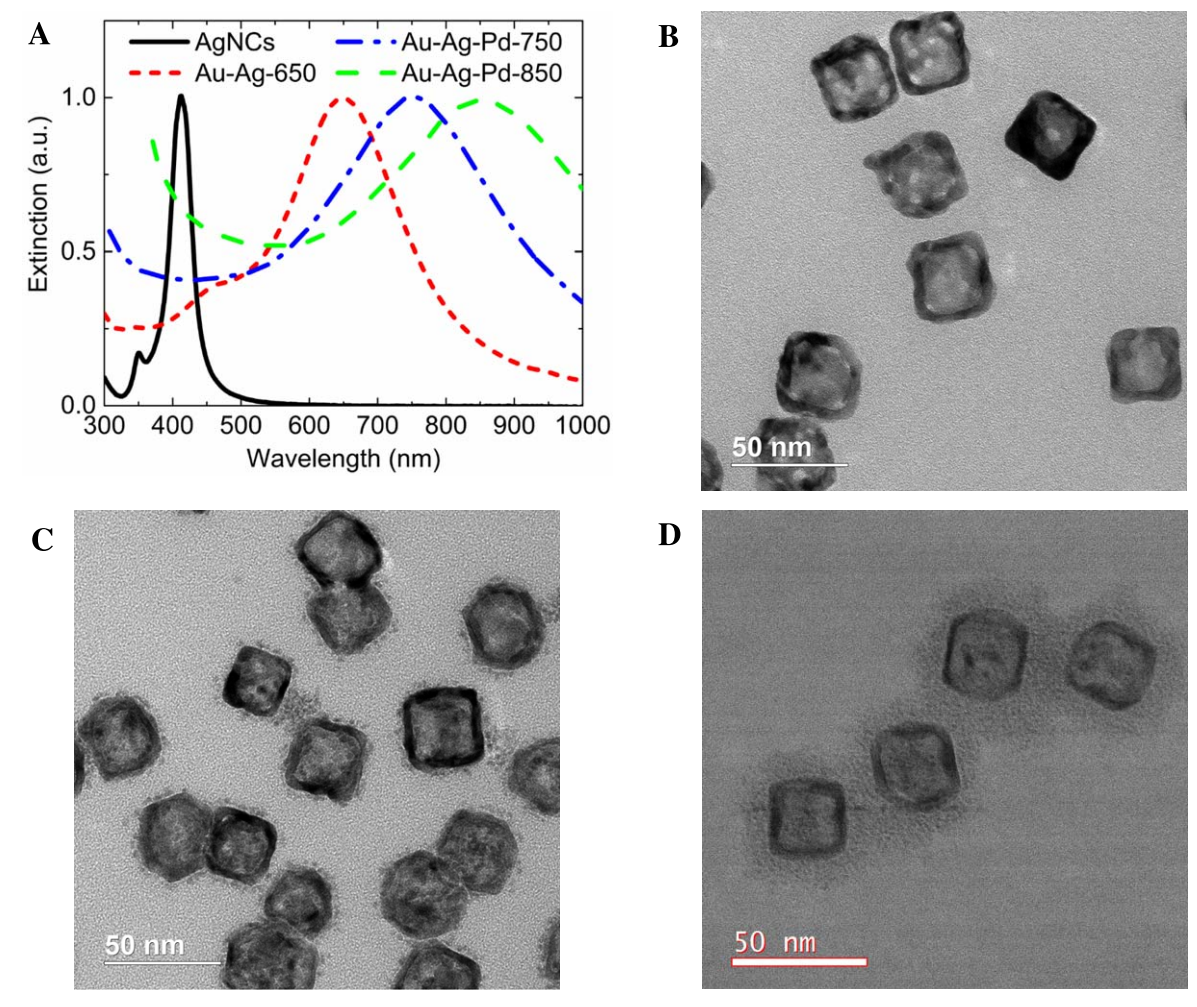


Figure 1. UV-Vis extinction spectra of silver nanocubes, bimetallic Au-Ag nanocages, and trimetallic Au-Ag-Pd nanoparticles with the LSPR peak positions at 750 nm and 850 nm. TEM images of (b) Au-Ag-Pd-750, (c) Au-Ag-Pd-750, and (d) Au-Ag-Pd-850. Silver nanocubes with the LSPR peak position at 412 nm are used as a template to synthesize various bimetallic and trimetallic nanoparticles.

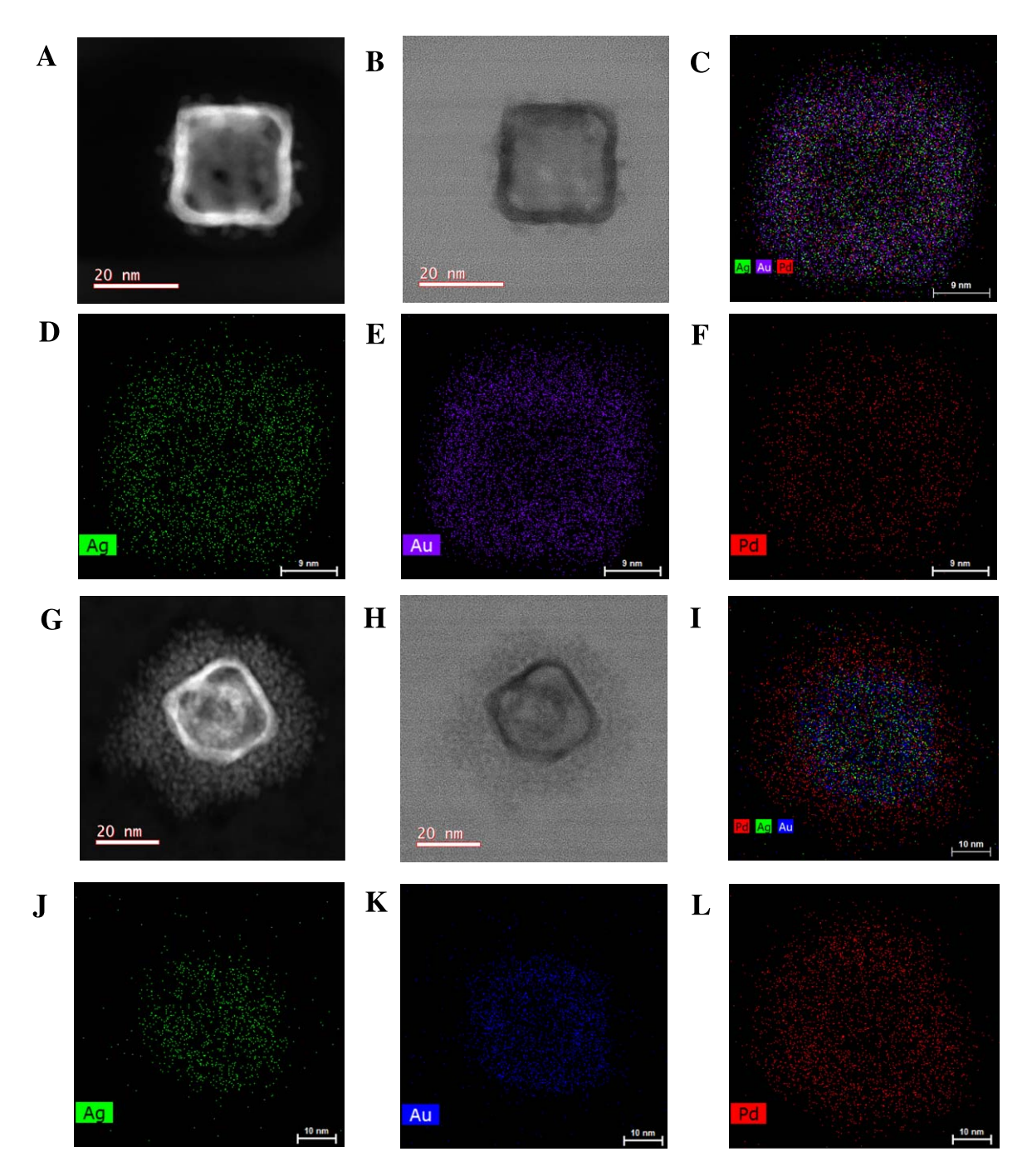


Figure 2. STEM (a), HRTEM (b), and EDX elemental mapping (c, d, e, f) of a representative single Au-Ag-Pd-750 nanoparticle. STEM (g), HRTEM (h), and EDX elemental mapping (i, j, k, l) of a representative single Au-Ag-Pd-850 nanoparticle.

LSPR peak redshifts to 750 nm and 850 nm. The stoichiometric balance between Ag and Pd $(Pd^{2+}_{(aq,)} + 2Ag^0_{(s)} \rightarrow Pd^0_{(s)} + 2Ag^+_{(aq,)})$ and the Pd and Ag contents in Table I reveal that the reduction of Pd^{2+} to Pd^0 is also accomplished through the island-growth mode on Au atoms (Fig. 2i). 30,31

X-ray photoelectron spectroscopy (XPS) results of Au-Ag-Pd-850 nanoparticles reveal a spin-orbit doublet for Au 4 f at 84.0 eV and 87.7 eV which is consistent with our prior study, indicating that the zero-valence state of Au (Au⁰) is preserved after the addition and reduction of the Pd²⁺ precursor in bimetallic Au-Ag nanocages (Fig. 3a). ²⁴ The Ag 3d doublet energy peaks at 367.9 eV and 373.9 eV slightly shifts to lower binding energy (0.2 eV) compared to the Ag 3d doublet in bimetallic Au-Ag nanocages; this is attributed to the interaction and charge distribution of metallic Ag⁰

and Pd precursors that occur after galvanic replacement (Fig. 3b). ³² The Pd 3d spectrum is deconvoluted into two pairs of doublets. The doublet peaks at 335.8 eV, and 340.8 eV correspond to Pd at zero-valence state, suggesting the successful incorporation of Pd⁰ in the bimetallic Au-Ag nanocages. The doublet peaks at higher binding energies and with lower intensities than those of zero-valence Pd metal (337.1 eV and 342.5 eV) are attributed to the oxidized Pd states (Pdⁿ⁺) (Fig. 3c). ³³ The X-ray diffraction (XRD) patterns of Au-Ag-Pd and Au-Ag nanocages indicate the presence of metallic Pd which is evident from the three distinct peaks at higher 2 θ angles (40.4°, 46.9°, 68.4°) in Au-Ag-Pd compared to those of the Au-Ag nanocages (38.3°, 44.6°, 64.7°) (Fig. 3d).

The electrochemical surface area (ECSA) of the Au-Ag-Pd nanoparticles is determined using a three-electrode cell with a

Table I. Au, Ag, and Pd concentrations of nanoparticles are determined by inductively coupled plasma emission spectroscopy (ICPES). The electrochemical surface areas (ECSA) of nanoparticles are determined based on the reduction peak of Au oxide and Pd oxide during CV measurements in Ar-saturated 0.1M LiOH solution at a scan rate of 50 mV s⁻¹.

Catalyst	Ag Conc. (μ g ml ⁻¹)	Au Conc. (μ g ml ⁻¹)	Pd Conc. ($\mu g \text{ ml}^{-1}$)	Au Content ^{a)} (at. %)	Pd Content (at. %)	$ECSA_{Au}\;(m^2\;g^{-1})$	$ECSA_{Pd} (m^2 g^{-1})$
Au-Ag-650	2.68	1.32	NA	21.25	NA	23.3	NA
Au-Ag-Pd-750	1.88	1.31	1.23	18.66	32.43	20.8	291.4
Au-Ag-Pd-850	1.35	1.29	2.77	14.52	57.72	22.2	345.4

a) atomic content is calculated using Au, Ag, and Pd concentrations divided by the molar mass of Au (196.97 g mol⁻¹), Ag (107.87 g mol⁻¹) and Pd (106.42 g mol⁻¹).

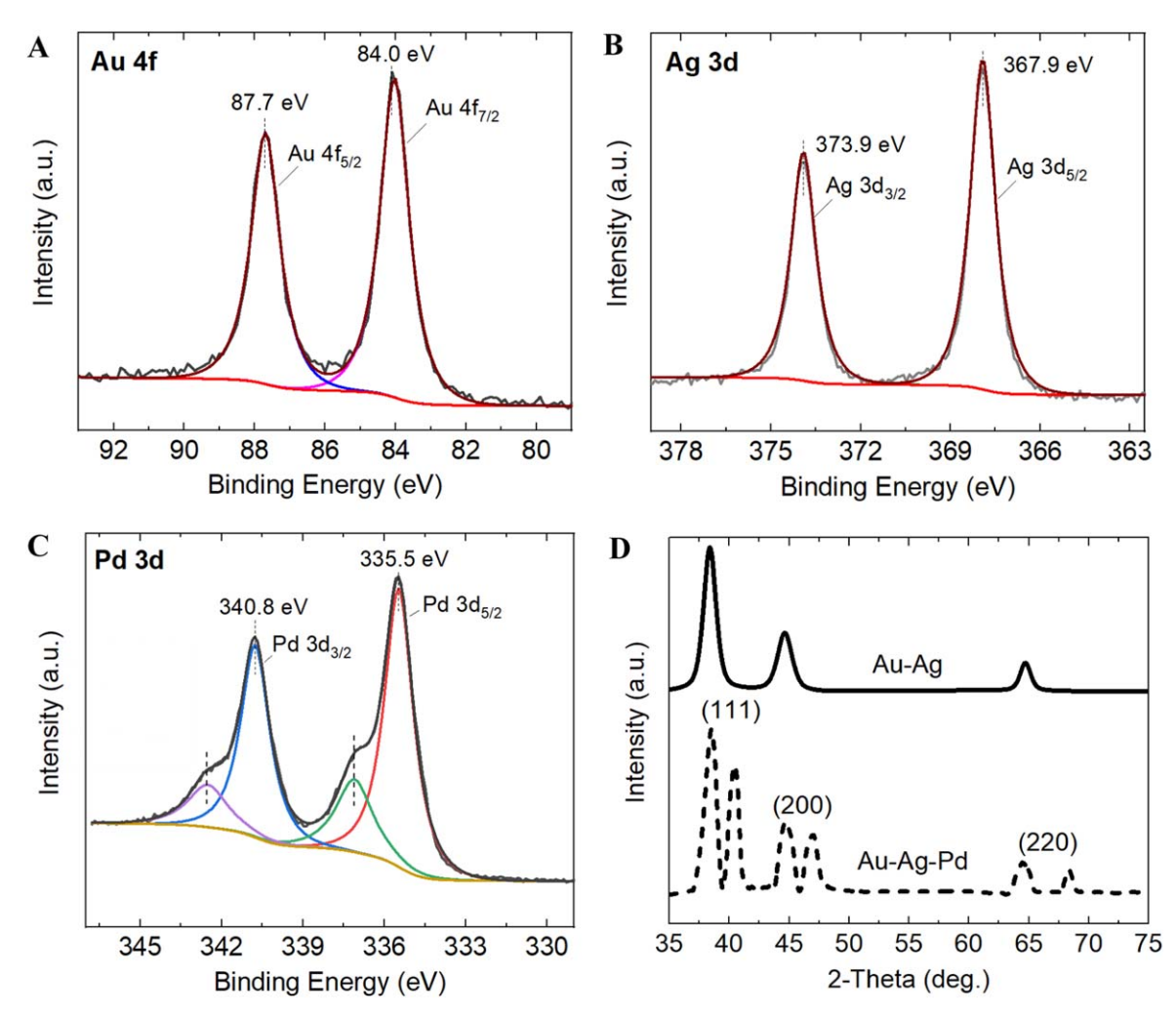


Figure 3. XPS spectra of (a) Au 4f, (b) Ag 3d, and (c) Pd 3d of Au-Ag-Pd-850 nanoparticles. All spectra were shift corrected using a standard reference C1s, C-C peak at 284.8 eV. (d) XRD pattern of Au-Ag and Au-Ag-Pd nanocages. The Pd diffraction peaks shift to higher 2θ angles due to the smaller lattice parameter (3.890Å) compared to those of Au (4.079 Å) and Ag (4.086 Å).

rotating disk electrode (RDE) and performing cyclic voltammetry (CV) in an Ar-saturated 0.1 M LiOH (aq.) at zero rotation rate at a scan rate of 50 mV s⁻¹. The ECSA_{Pd} is calculated from the reduction peak of Pd oxide after double-layer correction and a charge density of 424 μ C cm⁻²_{Pd} (Fig. 4a and Table I). The ECSAs of the nanoparticles are normalized to the Pd and Au loading on the working electrode, obtained from ICPES measurements (Table I). Au-Ag-Pd-850 has a higher surface area (345.4 m 2 g $^{-1}$) compared to the Au-Ag-Pd-750 (291.4 m 2 g $^{-1}$). This can be attributed to the existence of a thick porous layer of Pd at the exterior surface of the Au-Ag-Pd-850 nanoparticles, which increases the ECSA for catalytic reactions. It is well known that rough surfaces are catalytically more active than smooth surfaces, as atoms present on rough surfaces are more thermodynamically active. 30,34 The ECSA_{Pd} obtained using our trimetallic Au-Ag-Pd-850 nanoparticles is approximately five times higher than the ECSA_{Pd} of the commercial Pd/C catalysts. ^{17,35} Although the reduction peak area of Pd oxide is remarkably higher than that of Ag oxide, due to the comparable reduction potentials of these two metal oxides, the reduction peak area of Ag oxide is subtracted from the actual reduction peak area centered at around 0.5 V vs RHE to determine the ECSA_{Pd} (Fig. 4a). The observed negative shift in the electrochemical reduction of Pd oxide (\sim 0.1 V) in our trimetallic nanostructures, compared to the pure Pd, is attributed to the slight alloying of Pd and Ag at their interface during the galvanic replacement reaction. 36 The ECSAs_{Au}

of trimetallic Au-Ag-Pd nanoparticles is comparable (\sim 0.93) to the ECSAs_{Au} of bimetallic Au-Ag nanocages (Table I). ²² This indicates that the incorporation of Pd in bimetallic Au-Ag nanocages does not result in blocking the Au active sites for electrochemical NRR and confirms the preservation of the hollow structure in trimetallic nanoparticles where Au, Ag, and Pd can act as catalytically active centers for the reaction.

Linear sweep voltammetry (LSV) tests are performed in N₂-saturated 0.5 M LiClO₄ (aq.) electrolyte in an H-type cell, where a proton exchange membrane separates anodic and cathodic compartments. A neutral pH electrolyte was selected in this study based on our optimization of electrolytes' pH to obtain the highest electrocatalytic NRR activity.²² A remarkably higher current density is achieved using Au-Ag-Pd-750 and Au-Ag-Pd-850 nanoparticles compared to the bimetallic Au-Ag-715 nanocages (the best bimetallic Au-Ag nanocatalyst obtained in our previous study²²) (Fig. 4b). For instance, at an applied potential of -0.3 V vs RHE, the current density increases ~4.8 and ~3.7 times for Au-Ag-Pd-850 and Au-Ag-Pd-750 compared to the Au-Ag-715. This observation is consistent with significantly higher ECSA_{Pd} compared to the ECSA_{Au} (Table I) in trimetallic Au-Ag-Pd nanoparticles, which provides more active sites for nitrogen adsorption and reduction. Although achieving high current density at low overpotentials does not necessarily indicate the high selectivity and activity of an electrocatalyst toward NRR, it is the primary step toward the high production rate that is mandatory for

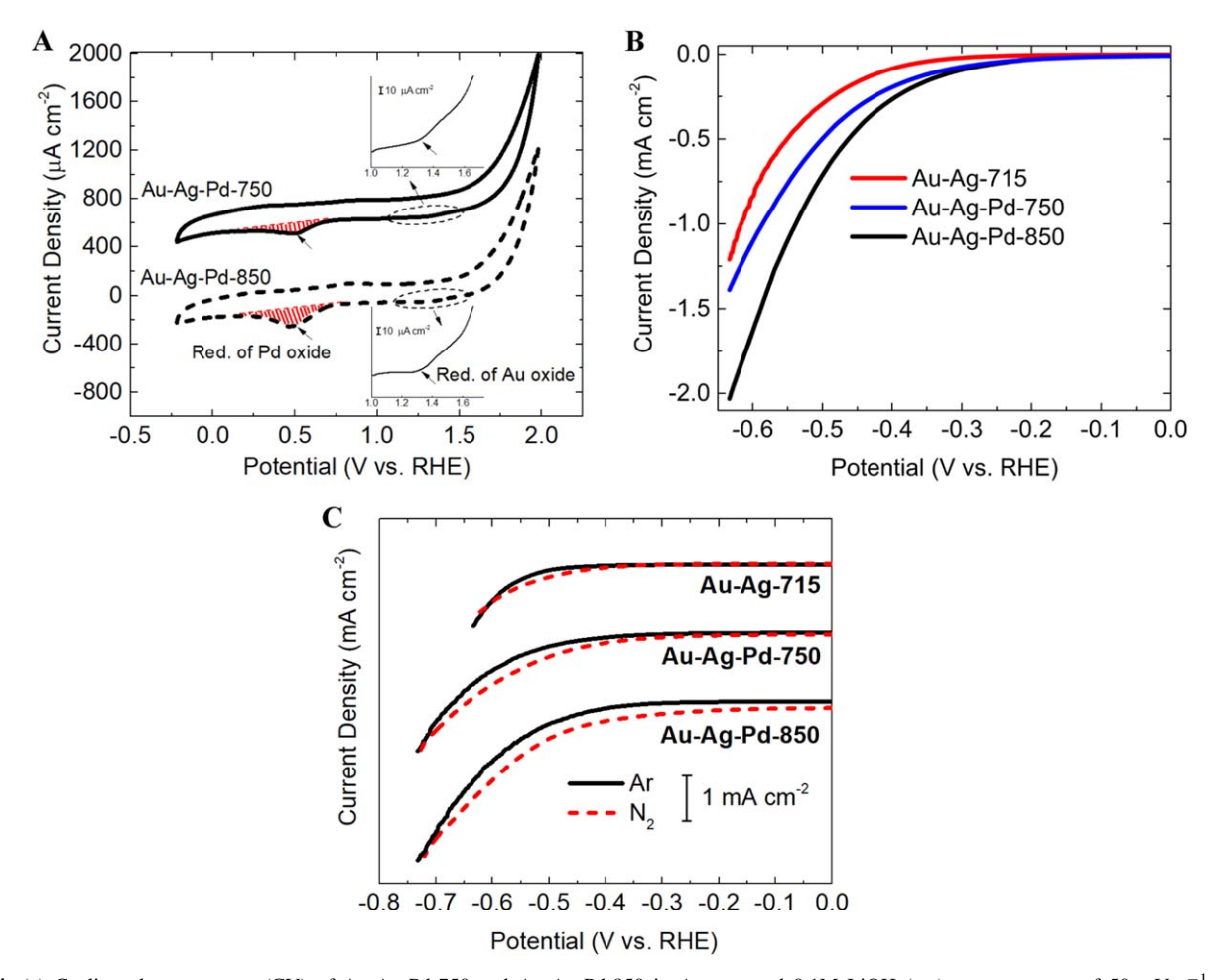


Figure 4. (a) Cyclic voltammograms (CV) of Au-Ag-Pd-750 and Au-Ag-Pd-850 in Ar-saturated 0.1M LiOH (aq.) at a scan rate of 50 mV s $^{-1}$. The CV measurements were conducted in the rotating disk electrode (RDE) setup at the stagnant electrode condition at room temperature. (b) Linear sweep voltammograms (LSV) of various catalysts in N₂-saturated 0.5 liClO₄ (aq.). (c) LSV tests of Au-Ag-Pd-750 and Au-Ag-Pd-850 in an Ar- and N₂-saturated 0.5 M LiClO₄ (aq.) under ambient conditions with the scan rate of 10 mV s $^{-1}$.

reaching the overarching goal of commercializing electrochemical NRR for sustainable ammonia production.

The selectivity performance $(\frac{I_{N_2} - I_{A_r}}{I_{N_2}} \times 100)$ of trimetallic Au-Ag-Pd nanoparticles is evaluated toward NRR. For both electrocatalysts (i.e., Au-Ag-Pd-750 and Au-Ag-Pd-850), the higher current density was achieved in N₂-saturated electrolyte compared, to the Ar-saturated electrolyte, within the wide potential window (Fig. 4c). Unlike the bimetallic Au-Ag nanocages demonstrated in our previous study,²² the selectivity performance of electrocatalysts improves at low overpotentials (0 V to -0.3 V vs RHE) toward NRR after the incorporation of Pd into the bimetallic Au-Ag nanocages (Fig. 4c). In addition, both electrocatalysts are selective toward NRR until the high negative potential of \sim -0.75 V vs RHE, even with an enhanced current density that is achieved using trimetallic nanostructures. This expands the selectivity of an electrocatalyst toward NRR in negative potentials by 0.15 V over that of Au-Ag nanocages. Moving toward more negative potentials than -0.75 V, a hydrogen evolution reaction (HER) becomes dominant. Here, we focus on the potential window of -0.3 to -0.5 V vs RHE, which is a compromise of obtaining high current density and selectivity. It is important to note that achieving a high current density for NRR is crucial to decrease the capital cost, leading to the commercialization of electrochemical NRR. At all three applied potentials, the selectivity is higher for Au-Ag-Pd-850 than for the Au-Ag-Pd-750; this is attributed to the higher Pd content and lower Ag content of Au-Ag-Pd-850 nanoparticles (Table II). Even though the selectivity is not substantially higher in trimetallic Au-Ag-Pd nanostructures than in the bimetallic Au-Ag nanocages, due to the enhanced current density obtained (I_{N_2}) using Au-Ag-Pd nanoparticles, the corresponding current density toward NRR $(I_{N_2} - I_{Ar})$ is much more pronounced after incorporation of Pd into Au-Ag nanocages.

Chronoamperometry (CA) tests are performed at a series of applied potentials using Au-Ag-Pd-750 and Au-Ag-Pd-850 nanoparticles to determine the ammonia yield rate and FE (Figs. 5a and 5b). The highest ammonia yield rate (13.74 μ g cm⁻² h⁻¹) is obtained at -0.4 V corresponding to an FE of 44.11% while the highest FE (48.94%) is achieved at -0.3 V (ammonia yield rate = 5.80 μ g cm⁻² h⁻¹) using Au-Ag-Pd-850. The higher ammonia yield rate but lower FE at -0.4 V, compared with -0.3 V, is attributed to the compromise between increasing current density and competitive selectivity toward HER rather than NRR. For all potentials tested, both the NH₃ yield rate and the FE are higher when Au-Ag-Pd-850 is used than when Au-Ag-Pd-750 is used. This result suggests that Pd content and ECSA_{Pd} of nanoparticles have a role in promoting the electrocatalytic NRR activity (Fig. 5b). In addition, greater Pd content in Au-Ag-Pd-850 compared to that of Au-Ag-Pd-750 results in an upshift of the d-band center $(E - E_f)$ from -4.45 eV to -3.73 eV, which was determined via ultraviolet photoelectron spectroscopy (UPS) measurements (Fig. S4, available online at stacks.iop.org/JES/167/ 054511/mmedia). This leads to improved binding strength of N-containing adsorbates with the catalyst surface, which is a crucial step for engineering selective and active NRR catalysts in an aqueous solution where selectivity is a major challenge.

Table II. Selectivity performance of trimetallic Au-Ag-Pd nanoparticles with LSPR peak positions at 750 nm and 850 nm toward NRR.

	Potential (V vs RHE)				
Electrocatalyst	-0.3	-0.4	-0.5		
Au-Ag-Pd-750	56.8	58.8	34.1		
Au-Ag-Pd-850	76.3	67.8	44.8		

Here, we also report the two critical parameters (i.e., production energy efficiency (%) and energy input (MWh $_{\rm Elec}$ /ton $_{\rm NH3}$)) in evaluating the performance of the N_2 electrolysis system, which is neglected in most electrochemical NRR studies in the literature. The highest production energy efficiency (28.9%) is achieved using Au-Ag-Pd-850 at -0.3 V, which corresponds to the electrical energy input of 19.1 MWh/ton $_{\rm NH3}$. Moving toward more negative potentials, the production energy efficiency decreases to 24.8% at -0.4 V and 8.3% at -0.5 V, mainly due to the significant increase in current

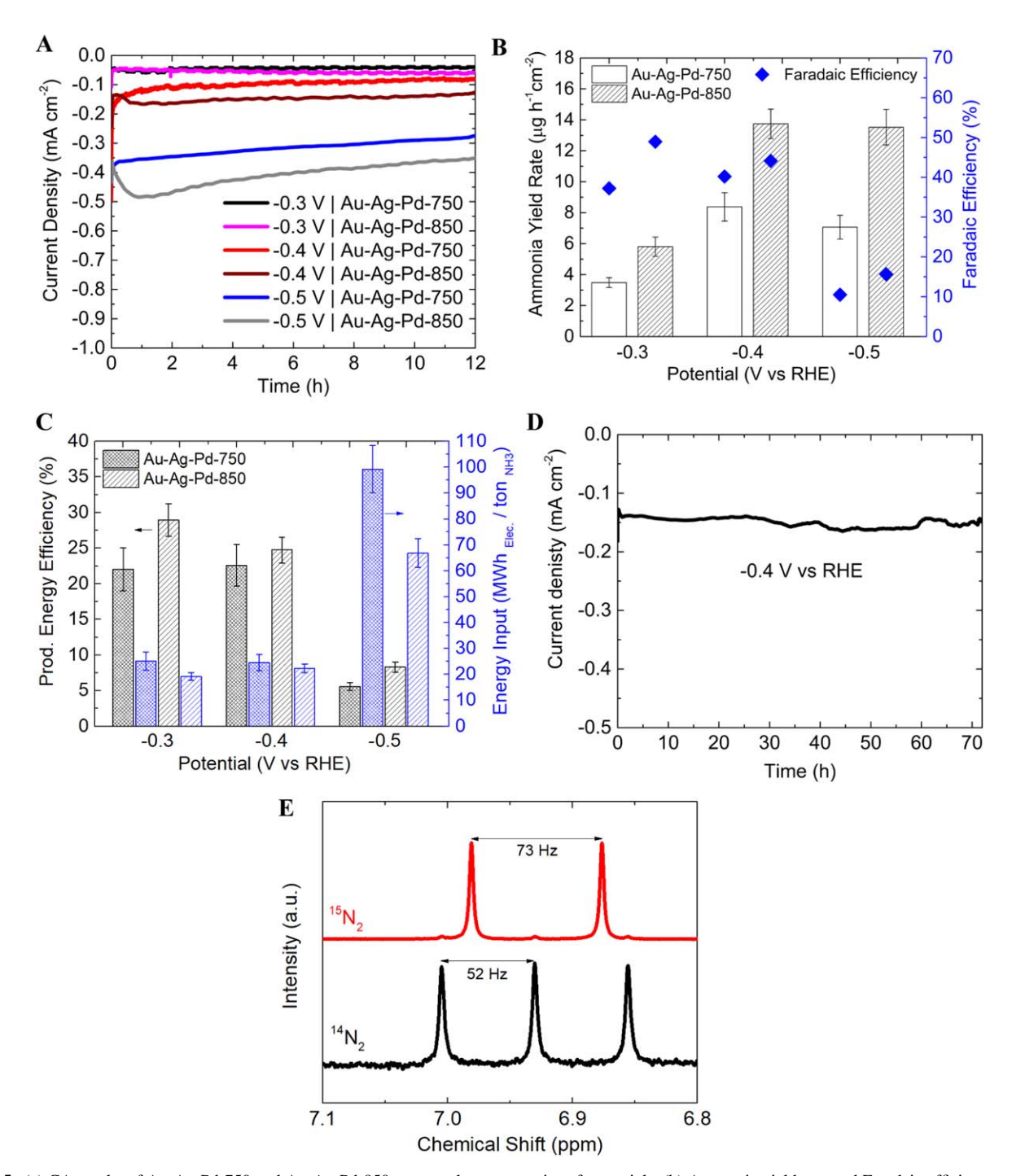


Figure 5. (a) CA results of Au-Ag-Pd-750 and Au-Ag-Pd-850 nanocatalysts at a series of potentials. (b) Ammonia yield rate and Faradaic efficiency at various potentials in 0.5 M LiClO₄ (aq.) solution using Au-Ag-Pd-750 and Au-Ag-Pd-850 nanocatalysts. (c) Production energy efficiency and energy input at various applied potentials using Au-Ag-Pd-750 and Au-Ag-Pd-850 nanocatalysts. The intense bars (black bars show production energy efficiency and blue bars show energy input) represent Au-Ag-Pd-750 and the medium bars represent Au-Ag-Pd-850. (d) CA test for the stability of the Au-Ag-Pd-850 at -0.4V vs RHE in 0.5 M LiClO₄ (aq.) solution. (e) 1 H-NMR spectra of samples after electrochemical 15 N₂ (14 N₂) reduction reaction at -0.4V vs RHE for 4 h in 0.5M LiClO₄ (aq.) solution.

density at more negative potentials, which increases the electrical energy input (Fig. 5c). It is noted that the increase in the production energy efficiency is in line with the decrease in the electrical energy input for various applied bias. Similar to the electrocatalytic NRR activity results (Fig. 5b), both production energy efficiency and energy input deteriorate for Au-Ag-Pd-750 compared to Au-Ag-Pd-850 in various applied potentials (Fig. 5c). Currently, a significant portion of the input electrical energy (>75%) for all conditions is consumed at the anode side, where oxygen evolution reaction (OER) takes place. Alternative use of organic-based electrolytes (e.g., glycerol) in the anodic half-reaction could remarkably lower the electricity consumption.³⁷ It is worth mentioning that the-state-of-the-art thermochemical process (Haber-Bosch) for ammonia synthesis consumes the energy of 7.8 MWh/ton NH3 (based on natural gas), and the target production energy efficiency of ARPA-E program (REFUEL) for electrochemical fuel production is greater than 60%.

A CA test is performed at -0.4 V for 72 h to evaluate the stability of Au-Ag-Pd-850 (Fig. 5d). The electrocatalyst could maintain the NH $_3$ yield rate (13.62 μg cm $^{-2}$ h $^{-1}$) and FE (43.5%) over 72 h, which is very close to the NRR activity of the catalyst in the initial 12 h test (Fig. S3a). This performance corresponds to the turnover frequency (TOF) of 59 h⁻¹ as per active Pd, Au, and Ag sites (see supporting information for the detailed calculation). The SEM images before and after the stability test, reveal that the nanoparticles are firmly attached to the substrate, and they are not washed away in long-term testing under stirring and applied bias (Fig. S1, Table SI). In addition, the TEM images after the stability test show the minor morphology change of nanoparticles after 72 h of the CA test (Fig. S2). Extensive control experiments are carried out following the instructions in the literature and our prior studies. ^{21,24,38–40} Control experiments (i.e., Ar, N₂ at OCV, N₂ with no catalyst) with conditions similar to those in Fig. 5b, yield remarkably smaller amounts of NH₃ (Ar: \sim 7.3% of N₂, N_2 at OCV: \sim 6.1% of N_2 , N_2 with no catalyst: \sim 2.5% of N_2) (Fig. S3b). The amount of ammonia produced in an isotopic labeling experiment using 15N2 gas after a 4 h electrolysis test is close to that of $^{14}N_2$ (73.6 μ M, \sim 91% of $^{14}N_2$) (Fig. S3c). Furthermore, the doublet and triplet couplings of ¹⁵N₂ and ¹⁴N₂ obtained from ¹H NMR measurement confirms that the supplied N2 is the major source of ammonia formation in the system (Fig. 5e). The amounts of ammonia measured using 1H NMR are similar to the indophenol method (71.9 μ M for $^{15}N_2$ and 78.4 μ M for $^{14}N_2$). Calibration curves of the H NMR signal and indophenol blue method for standard solutions of ¹⁵NH₄⁺ and ¹⁴NH₄⁺ were provided in our prior studies. ²¹

To probe the possible reaction mechanisms and track the intermediate species in electrocatalytic NRR, operando SERS spectra are collected during the CV tests on the SERS active substrate, which is comprised of Au-Ag-Pd nanoparticles deposited on the Au thin film working electrode. Detailed information regarding the spectroelectrochemical setup and CV curves is provided in the supporting information (Figs. S5 and S6). The SERS spectra in N2- and Ar-saturated LiClO₄ (aq.) solution contain the vibrational band located at 932 cm⁻¹, which is attributed to the stretching mode of the ${\rm ClO_4}^-$ anion (Figs. 6a and 6b). In addition, the wide vibrational band centered at 3415 cm $^{-1}$ corresponds to O–H stretching. As the potential is swept to negative values in the reductive pathway (0.97 V to -0.23 V vs $\hat{R}HE$), the faint evolution of three vibrational modes at 1094, 1393, 1601 cm⁻¹ is observed, reaching their highest intensity at −0.23 V; these can be classified as N–N stretching, H–N–H bending, and N-H wagging, and these suggest the formation of N₂H₄ as an intermediate species (Figs. 6a, 6c, 6d).²⁹ Two more peaks centered at 2937 cm^{-1} and 3605 cm^{-1} are evolved at -0.23 V, corresponding to the N-H asymmetric and symmetric stretching modes, respectively. The evolution of these two peaks strongly supports the formation of $\mathrm{NH_4}^+$ during the reductive potential sweep. ^{29,41,42} By moving toward more negative potentials during the reductive CV scan (-0.23 v to)-0.63 V), the intensity of peaks at 1094, 1393, 1601 cm⁻ (intermediates) decreases while the peak at 2937 cm⁻¹ and the shoulder at 3605 cm⁻¹ (NH₄⁺) reach their highest intensities. This strongly suggests the formation of NH₃ from the intermediate species

 $(N_2 \rightarrow N_2H_4 \rightarrow NH_3)$ (Figs. 6a, 6c, 6d). Since the literature values used to assign these peaks were obtained using infrared (IR) spectroscopy, the wavenumbers are not expected to align precisely, as the excitation mechanisms are different in each type of spectroscopy. The intensity of the peaks ascribed to intermediates and ammonium decreases during the oxidative pathway due to the oxidation of the N-containing species (Figs. 6a, 6c, 6d). The SERS spectra of the standard ammonia and hydrazine solutions in 0.5 M LiClO₄ (aq.) confirm the band assignment of various vibrational modes in NRR operando SERS measurements (Figs. S7 and S8). Furthermore, operando SERS measurements in Ar-saturated electrolyte with the electrocatalyst and N2-saturated electrolyte without the electrocatalyst reveal no pronounced peaks, implying the peaks observed in N₂-saturated electrolyte with the electrocatalyst are solely related to the formation of N-containing species at the presence of the electrocatalyst (Fig. 6b, Fig. S9).

Conclusions

The role of incorporating Pd in bimetallic Au-Ag nanocages on the electrocatalytic NRR selectivity and activity was investigated. TEM, EDX, ICPES measurements, and stoichiometric balance revealed that the reduction of Pd²⁺ to Pd⁰ is accomplished through both an islandgrowth mode on Au as well as the galvanic replacement of Ag. The increase in the Pd content is controlled by monitoring the localized surface plasmon resonance (LSPR) peak position of the resulting trimetallic nanoparticles. The ECSA_{Pd} achieved with our synthesized Au-Ag-Pd-850 nanoparticles is approximately 5 times higher than that of commercial Pd/C catalyst, which is mainly attributed to the formation of a rough and porous layer of Pd in trimetallic nanostructures. The correlation between the position of the d-band center of trimetallic nanoparticles and the Pd content was explored. Furthermore, the effect of Pd content on NRR current density, selectivity, and activity was discussed. The highest electrocatalytic NRR activity (FE = 48.94% and NH₃ yield rate= $5.80~\mu g~cm^{-2}~h^{-1}$) was achieved at -0.3~V vs RHE. This corresponds to the production energy efficiency of 28.9% and the electrical energy input of 19.1 MWh/ton NH3. Operando SERS revealed that electrochemical NRR takes place on the catalyst surface through an associative mechanism with N₂H₄ as an intermediate species.

This work highlights the importance of engineering the morphology and composition of nanocatalysts to improve the electrocatalytic NRR activity. In particular, it informs the crucial role of Pd with enhanced ECSA for increasing the rate of ammonia electrosynthesis. It also demonstrates the use of operando SERS as a powerful technique for unraveling reaction mechanisms for the electrocatalytic phenomenon.

Experimental

Nanoparticle synthesis.—Bimetallic porous Au-Ag nanocages with an LSPR peak position at 650 nm are synthesized by adding HAuCl₄ (aq.) solution to a solid silver nanocubes (AgNCs) solution through the galvanic replacement method.^{21–24} The Au-Ag nanocages are cleaned by centrifugation two times at 10,000 rpm for 10 min. Then, K₂PdCl₄ (0.006 M (aq.)) is gradually injected to the 100 ml Au-Ag solution (0.5 ml per 5 min) at room temperature (20 °C) under constant shaking in a 150 ml round-bottomed flask until the LSPR peak positions redshifts to 750 nm and 850 nm (approximately 1.5 ml of K₂PdCl₄ (aq.) for Au-Ag-Pd-750 and 2.5 ml of K₂PdCl₄ for Au-Ag-Pd-850). Unlike the galvanic replacement of Au³⁺ ions and Ag that takes place at the water boiling temperature, the galvanic replacement of Ag with Pd²⁺ takes place at room temperature, as the reaction of Pd ions with Ag is more active compared to that of the Au ions. The resulting trimetallic Au-Ag-Pd nanoparticles are washed two times by centrifugation at 12,000 rpm for 10 min. The precipitated nanoparticles are dispersed in DI water for future use.

Production energy efficiency calculation.—The production energy efficiency (η_{PEE}) of the electrolysis system is calculated according to the following equation:

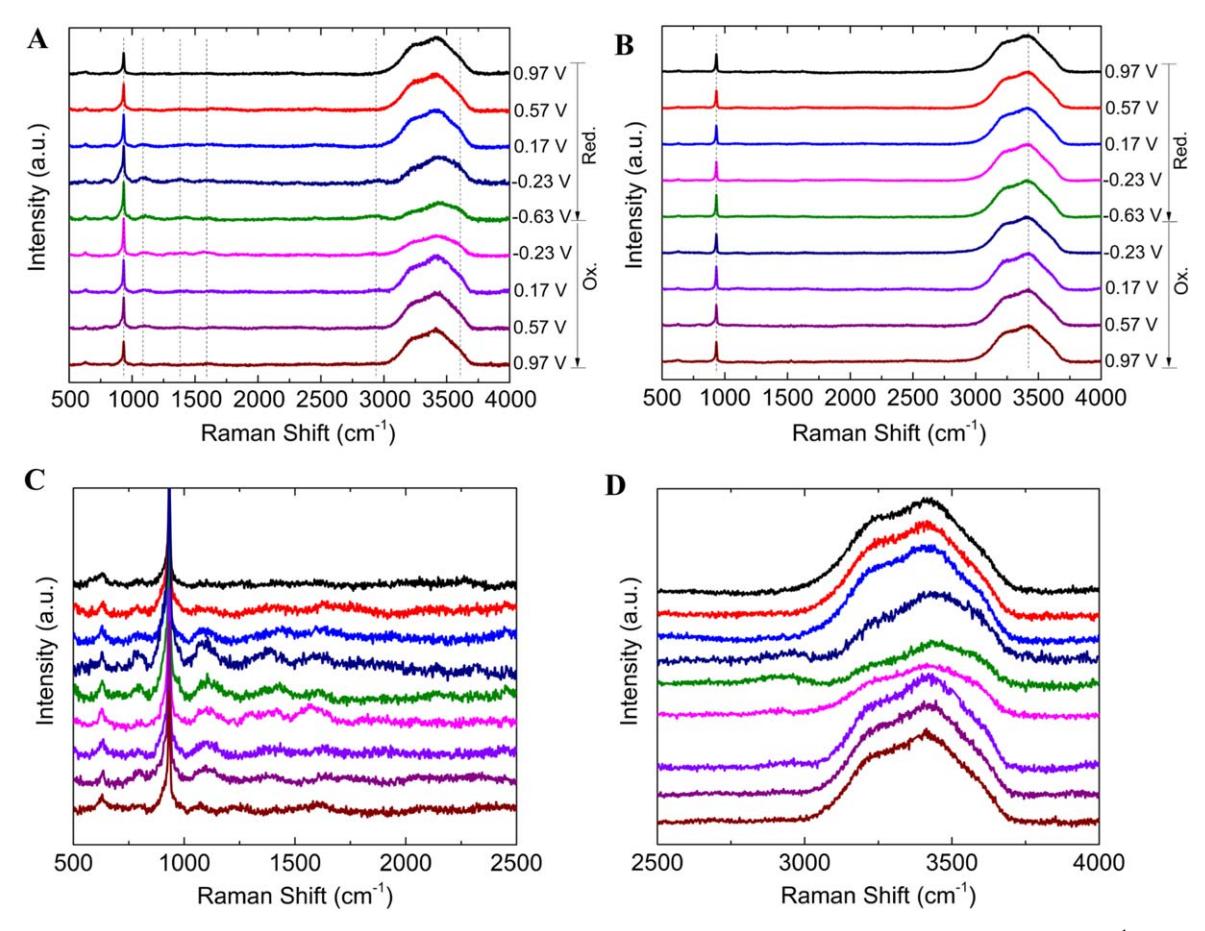


Figure 6. (a) Operando SERS using Au-Ag-Pd-850 nanoparticles in N_2 -saturated 0.5 M LiClO₄ (aq.) solution at the scan rate of 2.5 mV s⁻¹ with 532 nm laser. (b) Operando SERS using Au-Ag-Pd-850 nanoparticles in Ar-saturated 0.5 M LiClO₄ (aq.) solution at the scan rate of 2.5 mV s⁻¹ with 532 nm laser. (c) and (d) Low and high Raman shift of SERS spectra in N_2 -saturated electrolyte (Fig. 6a).

$$\eta_{PEE}(\%) = \frac{\Delta G \text{ for ammonia generation } (J \text{ mol}^{-1}) \times \text{ammonia generated } (mol)}{\int IV dt(J)} \times 100$$
 [1]

The free energy for NH₃ generation (ΔG) is 339 kJ mol⁻¹ and $\int IVdt(J)$ is the electricity consumed in the process (energy input). Here, V (V) is the full cell potential and is calculated according to the following equation:

$$V = (E_{anode} - E_{cathode}) + IR$$
 [2]

The cathode potentials (NRR) were measured in the three-electrode set up for each condition (Fig. 5c). The anode potential is estimated as the sum of the thermodynamic potential for water oxidation (1.23 V vs RHE) and OER overpotential (\sim 0.45 V on the Pt mesh).

The resistance (R) between anode and cathode in our setup is measured to be 75 Ω . This indicates that even for the case with the highest average current density (\sim 0.4 mA cm $^{-2}$ at -0.5 V vs RHE using Au-Ag-Pd-850), the resistive losses (IR) will be \sim 30 mV.

Determination of the electrochemical surface area (ECSA) of the nanoparticle.—The ECSA of the catalyst is determined from the charge associated with the reduction peak of Pd oxide (PdO) after double-layer correction and is normalized to the Pd loading on the working electrode and the charge density of $424 \mu C \text{ cm}^{-2}$ according

to the following equation³⁵:

$$ECSA\left(\frac{cm_{Pd}^{2}}{g_{Pd}}\right) = \frac{Q(\mu C cm^{-2})}{424 \ \mu C \ cm_{Pd}^{-2} \times electrode \ loading(g_{Pd} \ cm^{-2})}$$

where Q (μ C cm⁻²) is the charge associated with the reduction peak of Pd oxide after double-layer correction and is calculated according to the following equation:

$$Q = \frac{\int iV}{v}$$
 [4]

where *i* is the current density (μ A cm⁻²), *V* is the potential (V), and ν (V s⁻¹) is the scan rate.

Acknowledgments

The authors gratefully acknowledge Amazon Catalyst at ECS grant for supporting this work. This work was performed in part at the Georgia Tech Institute for Electronics and Nanotechnology, a member of the National Nanotechnology Coordinated Infrastructure

(NNCI), which is supported by the National Science Foundation (Grant ECCS-1542174). Additional financial support is acknowledged from the National Science Foundation under Grant No. 1904351.

References

- 1. V. Smil, in Enriching the Earth: Fritz Haber, Carl Bosch, and the Transformation of World Food Production (MIT press, Cambridge, MA) (2004).
- V. Smil, "Detonator of the population explosion." Nature, 400, 415 (1999).
 Survery, U. G., in Mineral Commodity Summaries 2016: US Geological Survey. (US Government Publishing Office, Washington, DC) (2016).
- 4. Survey, U. G., in Mineral Commodity Summaries, 2009 (Government Printing Office, Washington, DC) (2009).
- 5. S. Giddey, S. Badwal, C. Munnings, and M. Dolan, "Ammonia as a renewable energy transportation media." ACS Sustain. Chem. Eng., 5, 10231 (2017).
- 6. R. Strait and M. Nagvekar, "Carbon dioxide capture and storage in the nitrogen and syngas industries." Nitrogen + Syngas, 303, 1 (2010).
- 7. G. Soloveichik, "Electrochemical synthesis of ammonia as a potential alternative to the Haber-Bosch process." Nat. Catal., 2, 377 (2019).
- 8. G. Qing and T. W. Hamann, "New electrolytic devices produce ammonia with exceptional selectivity." Joule, 3, 634 (2019).
- D. Bao, Q. Zhang, F. L. Meng, H. X. Zhong, M. M. Shi, Y. Zhang, J. M. Yan, Q. Jiang, and X. B. Zhang, "Electrochemical reduction of N₂ under ambient conditions for artificial N2 fixation and renewable energy storage using N2/NH3 cycle." Adv. Mater., 29, 1604799 (2017).
- 10. M. M. Shi, D. Bao, B. R. Wulan, Y. H. Li, Y. F. Zhang, J. M. Yan, and Q. Jiang, "Au sub-nanoclusters on TiO2 toward highly efficient and selective electrocatalyst for N2 conversion to NH3 at ambient conditions." Adv. Mater., 29, 1606550 (2017).
- 11. Q. Qin, T. Heil, M. Antonietti, and M. Oschatz, "Single-site gold catalysts on hierarchical N-doped porous noble carbon for enhanced electrochemical reduction of nitrogen." Small Methods, 2, 1800202 (2018).
- 12. J. Zheng, Y. Lyu, M. Qiao, R. Wang, Y. Zhou, H. Li, C. Chen, Y. Li, H. Zhou, and S. P. Jiang, "Photoelectrochemical synthesis of ammonia on the aerophilichydrophilic heterostructure with 37.8% efficiency." Chem, 5, 617 (2019).
- 13. X. Wang, W. Wang, M. Qiao, G. Wu, W. Chen, T. Yuan, Q. Xu, M. Chen, Y. Zhang, and X. Wang, "Atomically dispersed Au₁ catalyst towards efficient electrochemical synthesis of ammonia." *Sci. Bull.*, **63**, 1246 (2018).
- J. Yang, Y. Guo, W. Lu, R. Jiang, and J. Wang, "Emerging applications of plasmons in driving CO₂ reduction and N₂ fixation." Adv. Mater., 30, 1802227
- 15. F. Akagi, T. Matsuo, and H. Kawaguchi, "Dinitrogen cleavage by a diniobium tetrahydride complex: formation of a nitride and its conversion into imide species.' Angew. Chem. Int. Ed., 46, 8778 (2007).
- 16. T. Shima, S. Hu, G. Luo, X. Kang, Y. Luo, and Z. Hou, "Dinitrogen cleavage and hydrogenation by a trinuclear titanium polyhydride complex." Science, 340, 1549 (2013)
- 17. J. Wang, L. Yu, L. Hu, G. Chen, H. Xin, and X. Feng, "Ambient ammonia synthesis via palladium-catalyzed electrohydrogenation of dinitrogen at low overpotential." Nat. Commun., 9, 1795 (2018).
- 18. K. Kim, S. J. Lee, D. Y. Kim, C. Y. Yoo, J. W. Choi, J. N. Kim, Y. Woo, H. C. Yoon, and J. I. Han, "Electrochemical synthesis of ammonia from water and nitrogen: a lithium-mediated approach using lithium-ion conducting glass ceramics." ChemSusChem, 11, 120 (2018).
- 19. P. Wang, F. Chang, W. Gao, J. Guo, G. Wu, T. He, and P. Chen, "Breaking scaling relations to achieve low-temperature ammonia synthesis through LiH-mediated nitrogen transfer and hydrogenation." *Nat. Chem.*, **9**, 64 (2017).
- N. Lazouski, Z. J. Schiffer, K. Williams, and K. Manthiram, "Understanding continuous lithium-mediated electrochemical nitrogen reduction." *Joule*, 3, 1127 (2019).
- 21. M. Nazemi, S. R. Panikkanvalappil, and M. A. El-Sayed, "Enhancing the rate of electrochemical nitrogen reduction reaction for ammonia synthesis under ambient conditions using hollow gold nanocages." Nano Energy, 49, 316 (2018).

- 22. M. Nazemi and M. A. El-Sayed, "Electrochemical synthesis of ammonia from N2 and H₂O under ambient conditions using pore-size-controlled hollow gold nanocatalysts with tunable plasmonic properties." J. Phys. Chem. Lett., 9, 5160 (2018)
- 23. M. Nazemi and M. A. El-Sayed, "The role of oxidation of silver in bimetallic gold-silver nanocages on electrocatalytic activity of nitrogen reduction reaction." J. Phys. Chem. C., 123, 11422 (2019).
- 24. M. Nazemi and M. A. El-Sayed, "Plasmon-enhanced photo (electro) chemical nitrogen fixation under ambient conditions using visible light responsive hybrid hollow Au-Ag₂O nanocages." Nano Energy, 63, 103886 (2019).
- 25. J. K. Nørskov, T. Bligaard, B. Hvolbæk, F. Abild-Pedersen, I. Chorkendorff, and C. H. Christensen, "The nature of the active site in heterogeneous metal catalysis." Chem. Soc. Rev., 37, 2163 (2008).
- 26. O. Zandi and T. W. Hamann, "Determination of photoelectrochemical water oxidation intermediates on haematite electrode surfaces using operando infrared spectroscopy." Nat. Chem., 8, 778 (2016).
- Y. Deng and B. S. Yeo, "Characterization of electrocatalytic water splitting and CO₂ reduction reactions using in situ/operando Raman spectroscopy." ACS Catal., 7 7873 (2017)
- 28. Y. Deng, A. D. Handoko, Y. Du, S. Xi, and B. S. Yeo, "In situ Raman spectroscopy of copper and copper oxide surfaces during electrochemical oxygen evolution reaction: identification of CuIII oxides as catalytically active species." ACS Catal., 6. 2473 (2016).
- 29. Y. Yao, S. Zhu, H. Wang, H. Li, and M. Shao, "A spectroscopic study on the nitrogen electrochemical reduction reaction on gold and platinum surfaces." JACS, **140**. 1496 (2018).
- M. Mahmoud and M. El-Sayed, "Metallic double shell hollow nanocages: the challenges of their synthetic techniques." Langmuir, 28, 4051 (2012)
- 31. C.-W. Yi, K. Luo, T. Wei, and D. Goodman, "The composition and structure of Pd-Au surfaces." J. Phys. Chem. B, 109, 18535 (2005).
- 32. G.-T. Fu, C. Liu, Q. Zhang, Y. Chen, and Y.-W. Tang, "Polyhedral palladiumsilver alloy nanocrystals as highly active and stable electrocatalysts for the formic acid oxidation reaction." Sci. Rep., 5, 13703 (2015).
- 33. L. Nahar, A. A. Farghaly, R. J. A. Esteves, and I. U. Arachchige, "Shape controlled synthesis of Au/Ag/Pd nanoalloys and their oxidation-induced self-assembly into electrocatalytically active aerogel monoliths." Chem. Mater., 29, 7704 (2017).
- 34. M. A. Mahmoud, R. Narayanan, and M. A. El-Sayed, "Enhancing colloidal metallic nanocatalysis: sharp edges and corners for solid nanoparticles and cage effect for hollow ones." *Acc. Chem. Res.*, **46**, 1795 (2013).
- 35. J. Nash, X. Yang, J. Anibal, J. Wang, Y. Yan, and B. Xu, "Electrochemical nitrogen reduction reaction on noble metal catalysts in proton and hydroxide exchange membrane electrolyzers." J. Electrochem. Soc., 164, F1712 (2017).
- J. Chen, B. Wiley, J. McLellan, Y. Xiong, Z.-Y. Li, and Y. Xia, "Optical properties of Pd-Ag and Pt-Ag nanoboxes synthesized via galvanic replacement reactions." Nano Lett., 5, 2058 (2005).
- 37. S. Verma, S. Lu, and P. J. Kenis, "Co-electrolysis of CO₂ and glycerol as a pathway to carbon chemicals with improved technoeconomics due to low electricity consumption." Nat. Energy, 4, 466 (2019).
- 38. S. Z. Andersen et al., "A rigorous electrochemical ammonia synthesis protocol with quantitative isotope measurements." *Nature*, **570**, 504 (2019).
- 39. B. H. Suryanto, H.-L. Du, D. Wang, J. Chen, A. N. Simonov, and D. R. MacFarlane, "Challenges and prospects in the catalysis of electroreduction of nitrogen to ammonia." Nat. Catal., 2, 290 (2019)
- 40. L. F. Greenlee, J. N. Renner, and S. L. Foster, "The use of controls for consistent and accurate measurements of electrocatalytic ammonia synthesis from dinitrogen." ACS Catal., 8, 7820 (2018).
- 41. C. Li, T. Wang, Z. J. Zhao, W. Yang, J. F. Li, A. Li, Z. Yang, G. A. Ozin, and J. Gong, "Promoted fixation of molecular nitrogen with surface oxygen vacancies on plasmon-enhanced TiO2 photoelectrodes." Angew. Chem. Int. Ed., 57, 5278 (2018).
- 42. A. D. Fortes, I. G. Wood, D. Alfè, E. R. Hernández, M. J. Gutmann, and H. A. Sparkes, "Structure, hydrogen bonding and thermal expansion of ammonium carbonate monohydrate." Acta Crystall. Sect. B:, 70, 948 (2014).
- M. Nazemi, J. Padgett, and M. C. Hatzell, "Acid/base multi-ion exchange membrane-based electrolysis system for water splitting." Energy Technol., 5, 1191 (2017).